Data Driven Autocalibration for Swath Sonars

Tor Inge Birkenes Lønmo, *Member, IEEE,* Andreas Austeng, *Senior Member, IEEE,* Roy Edgar Hansen, *Senior Member, IEEE.*

Abstract

Sidelobes in swath sonar water column imagery can obscure targets of interest and create erroneous bottom detections. Differences between ideal and actual element responses limit the achievable sidelobe level for practical arrays. Therefore, removing or reducing the errors by calibration may reduce the sidelobe level. We examine an autocalibration technique for swath sonars that use data collected while mapping. Our method is based on the "Generalized Interferometric Array Response" (GIAR). The GIAR values are used to find point-like signals and maximized to estimate the amplitude and phase errors for each element. On simulated data this reduces the sidelobe level to below -50 dB. In the field we find the calibration estimate stable over ping groups and that most sidelobes improved by two dB or more. This suggest that GIAR calibration can work well when the calibration match the swath sonar system. However, some sidelobes are also unchanged or degraded by a few dB. An extended calibration model seems necessary to achieve further improvements in the field.

Index Terms

Autocalibration, swath sonar, GIAR, water column imaging, bathymetry, array signal processing

I. Introduction

Swath sonar water column imagery has a large field of applications, from bathymetry quality control [1] to imaging bubble flares [1]–[3] and water column layering [4]. A factor that often limits its uses is the sidelobe level. Sidelobes can obscure targets [5, Ch. 4], which especially reduces the usefulness of the water column imagery after the first bottom echo [1], [2]. Sidelobes

T.I.B. Lønmo is affiliated with the University of Oslo and Kongsberg Maritime AS. E-mail: toribi@ifi.uio.no.

A. Austeng is affiliated with the University of Oslo.

R. Hansen is affiliated with the University of Oslo and the Norwegian Defence Research Establishment (FFI).

This work is supported by the Norwegian Research Council (Project 241275).

can also affect bathymetry by creating faulty peaks for the amplitude detector, or degraded, lost, or misplaced detections when using split-beam [6], [7, Ch. 8.3].

Ideally, the sidelobe level can be set almost arbitrarily low by weighting the beamformer [8]. In practice, it is limited. The achieved sidelobe level for swath sonars is typically no lower than -25 to -30 dB [1], [7, Ch. 5.4.6.3]. This limit is caused by errors like element displacement, amplitude and phase mismatch, mutual coupling and non-linearities [9, Ch. 4.1], [10, Ch. 13], [11, Ch. 7, 12], [12], [13]. To achieve lower levels, calibration is necessary.

Calibration may also be helpful for using adaptive beamformers with swath sonars, as the adaptive beamformers are more sensitive to calibration errors [13], [14], [15, Ch 6.6]. We have recently shown that adaptive beamformers may improve swath sonar performance [14], [16], [17], and calibration may increase that benefit [14].

Most swath sonar calibration methods are targeted at system parameters like mounting angles and beampattern. The patch test handles integration and mounting parameters [18], [19]. Other methods are used to measure the overall beampattern and calibrate the backscatter level [20], [21]. Although important for their purposes, the corrections are applied after beamforming. Since sidelobes are determined in the beamforming step, such calibration methods cannot improve the sidelobe level. Other calibration methods are therefore needed.

There exist a range of possible methods for element calibration [13], [15, Ch. 8.11], [22], [23], with variable assumptions and error models. In principle, calibration could be performed routinely in a tank. This would, however, not account for any changes related to the ship-mount [24] or changed material properties, for example due to temperature or pressure [11, Ch. 2.9 and 5] , [25, Ch. 4.2.2]. Repeated tank calibrations are very costly and may be required if element calibration values drift over time. Such drift may be expected since it occurs for backscatter calibration [25, Ch. 5.2]. Environmental effects are also not included if calibrating via internal reference signals [26]. A field calibration method which includes the whole system is therefore desirable, preferably a method without the need for additional equipment like reference sources.

Calibration without known source locations is known as autocalibration or self-calibration [12, Ch. 3]. Autocalibration exists for general arrays [23], [12, Ch. 3.4], [15, Ch. 8.11.5] or for particular applications [27]–[29]. We considered a range of options and found “General Interferometric Array Response” (GIAR) based calibration [28] to be most promising. Key advantages are that the method is simple, compatible with typical signal conditions, and [28] showed indications of meaningful results on swath sonars.

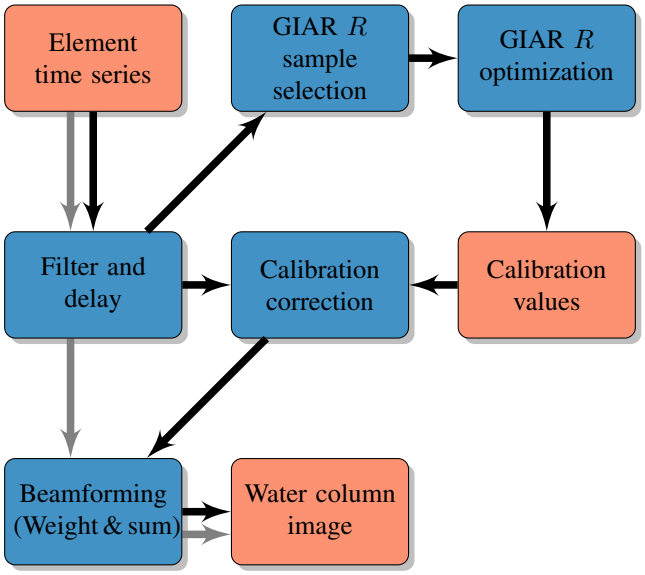

Fig. 1. Processing with calibration. Standard processing follows gray arrows. Calibration procedure in the upper right corner is described in Section IV. Note that DAS beamforming is spread across two blocks. The "Filter and delay" block calculates $\mathbf{s}(\theta, r)(t)$, while $\mathbf{w}^H \mathbf{s}(\theta, r)(t)$ is evaluated in the "Beamforming" block.

In [28], Cervenka outlined how GIAR could be used for autocalibration and showed consistent calibration results across three pings. The purpose of this paper is to provide a detailed performance evaluation of the outlined method. Our main contributions are a detailed description of how GIAR can be used for autocalibration of swath sonar receivers, quantification of accuracy and efficiency on simulated data, and demonstration and analysis of performance in the field.

The simulations show that GIAR can accurately estimate calibration errors using data from normal operation and that correction for them can reduce sidelobe level to below -50 dB. Field examples show stable error estimates in practice, however the resulting improvement in sidelobe level is around 1.2 dB on average and more variable. The reduced performance in the field seems to be caused by an insufficient calibration model.

In the following we present the signal model, GIAR, and the calibration procedure. We then show and discuss results from simulated and field data.

II. Swath sonar processing

The basis for our analysis is a standard swath sonar processing chain [7, Ch. 8.3]. The central parts are shown in Fig. 1. The Delay-and-Sum (DAS) beamformer [30, Ch. 4] is the key component for our purposes.

DAS beamforming is done by delaying the signal from each element, such that the array is steered toward a target direction (far-field) or point (near-field), and summing the result. For narrowband signals the delays may also be applied by phase rotation. Weighting (also called apodization, shading or tapering) is used to suppress interfering signals better by lowering the sidelobe level, at the cost of reduced resolution and lower white noise suppression [8]. The resulting beam time series $b^{(\theta,r)}(t)$ steered toward the angle θ and range r is given by

$$b^{(\theta,r)}(t) = \mathbf{w}^H \mathbf{s}^{(\theta,r)}(t) = \begin{bmatrix} w_1 \\ w_2 \\ \vdots \\ w_{N_{\text{El}}} \end{bmatrix}^H \begin{bmatrix} s_1^{(\theta,r)}(t) \\ s_2^{(\theta,r)}(t) \\ \vdots \\ s_{N_{\text{El}}}^{(\theta,r)}(t) \end{bmatrix}, \tag{1}$$

where N_{El} is the number of elements, w_i is the weight for element i, and $s_i^{(\theta,r)}(t)$ is the signal from element i at time t, after it has been delayed toward (θ, r), and $\bullet^H$ indicates the complex conjugate transpose. We will refer to the delayed signal vector $\mathbf{s}^{(\theta,r)}(t)$ as a "sample", as it is used as input for the calibration procedure. The steering angle θ is measured relative to the array normal. For simplicity, we will omit the steering angle, range, and time from now on, using s_i for $s_i^{(\theta,r)}(t)$.

In principle, the sidelobe level could be set as low as desirable by selecting an appropriate weight [8]. In practice, the achievable sidelobe level is limited by calibration errors [10, Ch. 13.6], [9, Ch. 4.3], [11, Ch 7.1.6]. Figs. 2 and 3 illustrate this by example.

The lower panels in Fig. 2 shows the phase ϕ_i and amplitude a_i of the complex calibration errors $c_i = a_i e^{j\phi_i}$ for each element. The plot at the top of Fig. 2 shows the effect on the beampattern when DAS is used on a signal with calibration errors $\tilde{s}_i = s_i c_i$. When errors are present the sidelobes are between -30 and -40 dB, instead of reaching below -60 dB as in the error-free case. The mainlobe, however, remains approximately constant. The mainlobe is generally less sensitive [10, Ch. 13.3-4], and we therefore focus on the sidelobes in this study.

Fig. 3 illustrates that the calibration errors effectively limit the sidelobe level. For this case it makes the sidelobe level largely independent of the weighting used. The exception is near the mainlobe where some ideal sidelobes exceed the sidelobe limit. This illustrates that the practical sidelobe level may be limited by the calibration errors or the ideal sidelobe level. To reveal the effect of calibration, it is important to use weights with low ideal sidelobe level.

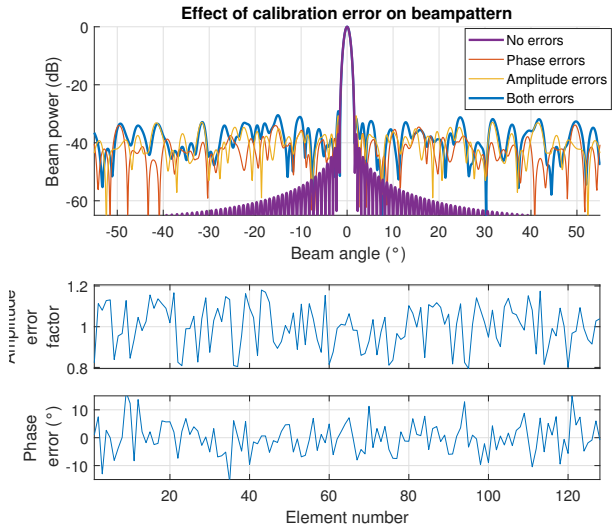

Fig. 2. Top: Effect of amplitude and phase calibration errors on a linear, 128-element, Kaiser $\beta = 5$ weighted array. Middle: Amplitude calibration error factors (multiplicative) used in the plot. Bottom: Phase calibration errors used in the plot. Amplitude errors are uniformly distributed within $\pm 20\%$. Phase errors were drawn from a normal distribution with 5° standard deviation.

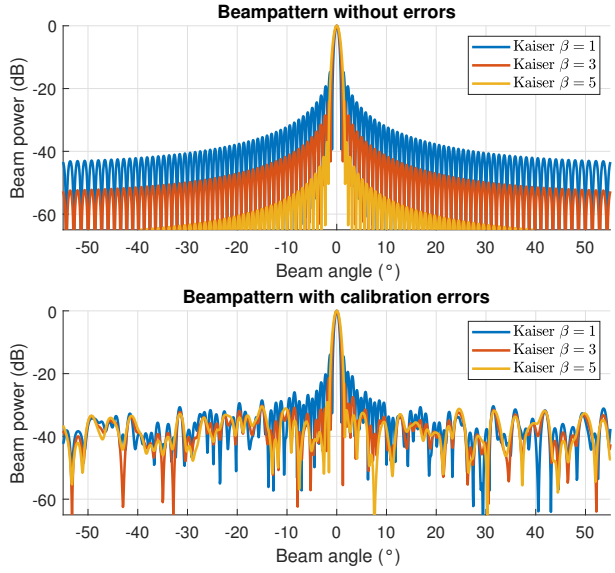

Fig. 3. Illustration of the sidelobe limiting effect of the calibration errors in Fig. 2. (Top) With ideal data, weighting the array reduce sidelobe level. (Bottom) With calibration errors, the sidelobe level is limited. All weights perform similarly when the error-free sidelobe level is about -35 dB or lower.

Dette er en postprint-versjon/This is a postprint version. Publisert versjon/Publised version: https://doi.org/10.1109/JOE.2020.3036184

In the following examples we use Kaiser weights [8] with $\beta = 5$, which has a maximal sidelobe of -37 dB and sidelobes below -60 dB outside $\pm 30^\circ$ degrees. Our parameterization differs from [8] through $\beta = \pi\alpha$. The low sidelobe level make the weight set well suited for the purposes of this paper, although the increased beamwidth and degradation of other weight properties may make them unsuitable for many applications. Note that the weights are only used during beamforming and do not affect the calibration process.

III. The Generalized Interferometric Array Response (GIAR)

GIAR was introduced in [28], [31] as an alternative interferometric method to split-beam. In [28], it was also suggested that GIAR might be used for calibration. This section describes the key properties of GIAR, how it is defined, and how we use it for calibration.

In essence, GIAR may be described as a combination of the coherence factor and split-beam. The amplitude of GIAR behaves similarly to the coherence factor, also called semblance, which is a measure of the similarity to an ideal signal from the steering direction. It is sensitive to phase and calibration errors [28], [32], [33] which means that maximizing the GIAR amplitude may be used to estimate calibration errors. The phase of GIAR behaves like the split-beam phase near the beam direction, it has a one-to-one relation with the arrival angle relative to the beam direction. In contrast to split-beam, the phase of GIAR does not have ambiguities near the steering direction [31]. We use these properties to compensate for the predicted loss in GIAR amplitude due to difference between the steering and arrival angle and to reject samples outside the mainlobe.

The GIAR C is defined as the average of all unique inter-element cross products,

$$Q = \frac{2}{N_{\text{El}}(N_{\text{El}}-1)} \sum_{i=1}^{N_{\text{El}}-1} \sum_{j=i+1}^{N_{\text{El}}} s_i s_j^H, \tag{2}$$

normalized by the average element power,

$$E^2 = \frac{1}{N_{\text{El}}} \sum_{i=1}^{N_{\text{El}}} |s_i|^2. \tag{3}$$

That is $C = Q/E^2$. When viewed in terms of the covariance matrix $\mathbf{s}\mathbf{s}^H$, Q is the average of everything above the diagonal and E is the average of the diagonal.

As in [28] we normalize C by the GIAR Point Spread Function (PSF) C_{PSF}, the GIAR response to an ideal far field signal. This removes the effect of the signal direction on the

GIAR amplitude for ideal signals near the steering direction. Since the sample selection method described in the next section rejects samples outside the central mainlobe, the normalization may be done via the following approximation of C_{PSF} [31]:

$$\begin{aligned} C_{PSF}(\xi) &\approx \operatorname{sinc}^2 \frac{\xi}{\sqrt{3}} e^{j2\pi\xi/3}, \text{ where} \\ \xi &= \frac{d}{\lambda}(\sin\phi - \sin\theta), \quad \operatorname{sinc} x = \frac{\sin \pi x}{\pi x}, \end{aligned} \tag{4}$$

d is the element separation, λ is the wavelength, ϕ is the angle between the signal direction and the array normal. The approximation is accurate when $|\xi| < 0.7$ [31]. The normalized GIAR value is then:

$$R = \frac{C}{|C_{PSF}(\xi_0)|}, \tag{5}$$

where ξ_0 is the value where the phase of $C_{PSF}(\xi_0)$ is equal to the phase of C. Note that the phase of R is the same as the phase of C.

IV. GIAR AUTOCALIBRATION PROCEDURE

This procedure is based on the description in [28]. The procedure has two main steps, sample selection and optimization.

In short, we first use the amplitude and phase of R to find samples which resemble point-like signals from near the steering direction. We then find calibration values that maximize the average $|R|$, since $|R|$ is maximized for an ideal signal arriving at a calibrated array.

For sample selection we do the following for all available pings:

1) Delay samples for all wanted beam angles and ranges.
2) Calculate R for all delayed samples.
3) Select all samples with $|R| > R_{min}$ and $|\angle R| < \eta_{max}$, where $\angle R$ is the phase of R.
4) Merge clusters of accepted samples: If samples adjacent to each other are accepted in step 3, keep only the sample with highest $|R|$.

Step 4 is not in [28]. We added it since we expect the samples within a cluster may be correlated. In our tests we found that this choice reduced run-times and had only a small effect on the result. We use $R_{min} = 0.8$ and $\eta_{max} = 0.5$ rad $\approx 30°$, which give a region of acceptance as shown in [28, Fig. 4]. Note that the caption of [28, Fig. 4] states $\eta_{max} = 0.25$, while the figure match $\eta_{max} = 0.5$. We use the larger value since we found that it increased the number of accepted samples without reducing performance.

After N_S accepted samples are found during sample selection, the final autocalibration step is:

- Find $\hat{\mathbf{c}} = [\hat{c}_1, \ldots, \hat{c}_{N_{\mathrm{El}}}]$ that maximize mean $|R|$ after correcting all samples with $\hat{c}$, that is $\hat{s}_i = \tilde{s}_i / \hat{c}_i$, under the constraints that $\hat{\mathbf{c}}$:
  - Has no linear trend in phase. (That is, preserve beam pointing angles)
  - Preserve average element amplitude. (That is, preserve absolute backscatter levels).

As a safety measure we also required the calibration changes to be less than 90° in phase and 50% in amplitude. The calibration values $\hat{\mathbf{c}}$ are initialized to unity, as the best guess without further information. We found that the optimization result was independent of the initial value when testing other options.

The optimization step was implemented in MATLAB [34] using the function `fmincon` found in the Optimization toolbox. The resulting calibration values can be corrected for elementwise at any step before beamforming.

V. Simulation method

We have used simulated data to evaluate the method in a controlled environment. Our simulation program is built around Field II [35]–[37], a point-based simulator well regarded in the medical ultrasound community. Field II can provide element time series for a given set of point scatterers, transmit, and receive arrays.

We model the seafloor segments as a collection of points with uniform directivity and Gaussian scattering strength. The points are initially distributed in a grid to ensure sufficient coverage of every resolution cell, and then perturbed in all directions to ensure random phase. Table I lists the seafloor geometries we have simulated. Our grid has 4 rows along-track with approximately 12 cm spacing. The spacing between across-track columns are approximately 36 mm. The minimum number of points per resolution cell is 8.

The simulated array has a Mill's cross geometry [7, Ch. 8.3.2]. The receiver is a linear array with 128 $\lambda/2$-elements. For faster simulations the transmitter is modeled as a single element. To recreate the along-track beamwidth, the extent of the seafloor is limited to 0.7°. White gaussian noise is added to the simulated element data before doing receiver processing. These and the remaining parameters are summarized in Table II. The parameters were chosen based on [7, Ch. 2.3.2 and Ch. 8.3] and historical survey data. We have not adjusted the absolute scattering strength to physically meaningful levels since only relative values are important for this study.

TABLE I

DEPTH AND SHAPE FOR SIMULATED SEAFLOOR SCENES.

Scene #	Description
0	Flat, stepped, seafloor at 39 and 40 m depth. Switch at every 5m.
4	Flat seafloor, depth 40 m.
	Sinusoidal seafloors, mean depth 39.5 m:
	(P is the period [m], A is the amplitude [m])
1	$P = 5$, $A = 0.5$.
2	$P = 8$, $A = 0.5$.
3	$P = 8$, $A = 0.25$.
6	$P = 2.5$, $A = 0.25$.
7	$P = 1$, $A = 0.1$.
8	$P = 1$, $A = 0.05$.
9	$P = 10$, $A = 0.5$.
	Sinusoidal seafloor, mean depth 80 m:
5	$P = 0.5$ $A = 5$.

We have used the same noise level across all scenes. For the flat seafloor (scene 4) the element SNR ranges from roughly 20 dB for the vertical direction to -5 dB at 40 degrees.

VI. SIMULATION RESULTS

We simulated series of 100 pings for all seafloors listed in Table I. Each ping was processed, and samples suitable for calibration were selected according to the procedure in Section IV. We ran GIAR autocalibration on individual pings, ping series, and all available data to investigate the performance. To better show the sidelobe structure, we omitted additive noise when showing water column images. As described in Section V, noise is always included when estimating the calibration parameters.

Fig. 4 and 5 illustrate the effect of autocalibration on the beampattern, the water column image, and the effect of more data. The lower panels in Fig. 4 show a large reduction in the error for the single ping estimate. The calibration errors shown in the lower panels are greatly reduced for the single ping estimate, and are further reduced when calibrating on all data. The upper panel shows that the single ping estimate lowers the sidelobes from about -30 dB to roughly

TABLE II

SIMULATION PARAMETERS

Parameter	Value
Center frequency	300 kHz
Pulse length	100 μs
Pulse type	CW
Pulse shaping	Hanning [8]
Sound speed	1500 m/s
Depth	See Table I
Number of elements	128
Element spacing	$\lambda/2$
Attenuation	65 dB/km
Transmit beamwidth	$0.7^\circ \times 120^\circ$
Simulation region	$\pm 60^\circ$ across-track

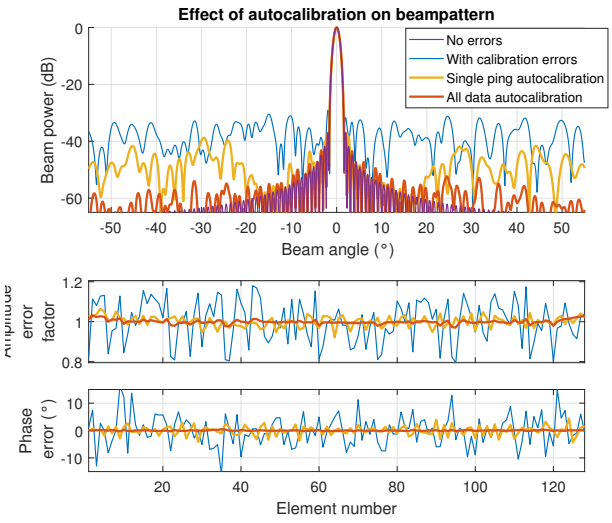

Fig. 4. Effect of autocalibration on beams from example in Fig. 2. The single ping estimate is based on 91 accepted samples from scene 2. The all data estimate is based on 72177 accepted samples collected from all scenes in Table I. Fig. 5 shows the effect on the water column image. Noiseless data used for the beam plot. Data with noise used for autocalibration. Same colormap is used in all plots.

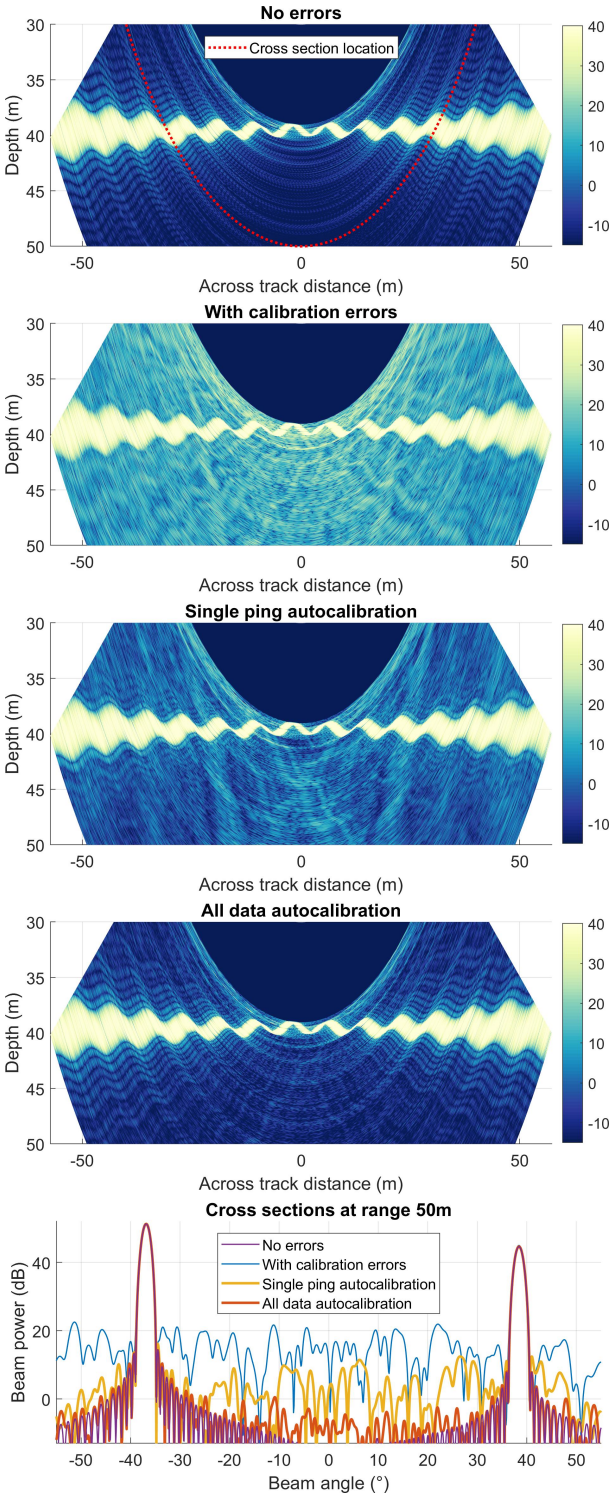

Fig. 5. Effect of GIAR autocalibration on the water column image from a simulated ping from Scene 2. Same calibration data as in Fig. 4. Cross section range indicated by the red dotted line in the "No errors" plot. The color scale show beam power in dB, with range clipped above to show sidelobes better. Noiseless data used for these plots. Data with noise used for autocalibration.

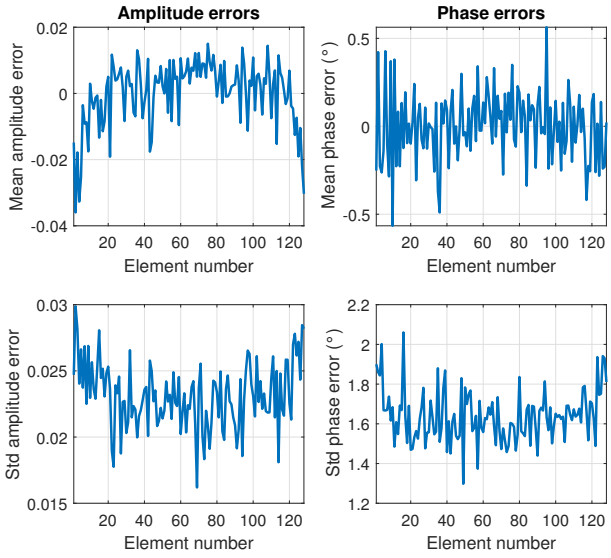

Fig. 6. Per element autocalibration error mean and standard deviation (std) for per ping calibration of 100 pings from scene 2.

-40 dB. The full calibration lowers the sidelobe level by an additional 10-15 dB, leaving most sidelobes below -50 dB and many below -55 dB.

Fig. 5 shows the effect of autocalibration on the water column image. In the water column the sidelobe level is improved with the single ping estimate, and looks comparable to the ideal image when calibrating on all data. The cross section in Fig. 5 also shows great similarities to the ideal beampattern in Fig. 4.

Fig. 6 shows the observed mean and standard deviation of the calibration corrections when autocalibration is performed separately on each of the 100 pings from scene 2. The mean amplitude errors show some structure. The edge elements tend to have a lower estimate than the center elements, and have values comparable to the standard deviation. For the phase, the magnitude of the mean values is about a tenth of the standard deviation. For both phase and amplitude, the standard deviation is somewhat higher toward the edges. The results from other scenes are similar.

For 100 independent realizations the standard deviation of the mean can be expected to be a tenth $(1/\sqrt{100})$ of the standard deviation for the individual values [38]. This means that the mean amplitude error for the edge elements are about ten times higher than the expected standard deviation, which suggests that this is a real bias. For the phase error, the mean value has variations at the scale of the expected standard deviation, which appear consistent with an

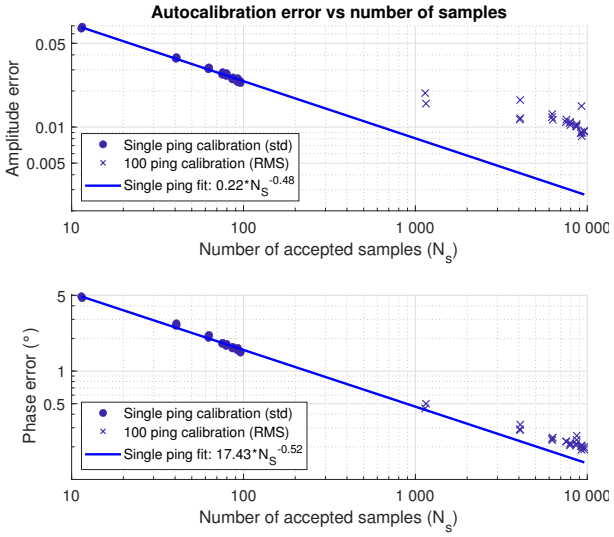

Fig. 7. Estimation error vs number of accepted samples used for autocalibration. The circles show standard deviation (std) of autocalibration error across all elements after removal of the per-element bias. Similar to the average standard deviation across all elements in Fig. 6 for all scenes. Each circle is calculated on 100 pings on a single scene. Note that the average number of samples accepted N_S varies between scenes. The crosses show the root-mean-square (RMS) error across the array for autocalibration all 100 pings combined per scene. Bias is included in the RMS value. The single ping error fit is the best power law fit (aN_S^b) to the single ping error estimates.

unbiased phase estimate. The higher standard deviation for the edge elements may indicate that these are harder to estimate, but further analysis is required to determine if this is a real effect. We have not formally evaluated if these effects reach statistical significance since they, even if real, do not have practical significance at this stage. The sidelobe levels achieved in Fig. 5, which include these effects, are far better than the field results presented in the next section. Therefore, other effects are currently limiting performance. In addition, note that an amplitude bias may be removed by other methods, for example by equalizing the average power per element [29].

Fig. 7 shows the number of accepted samples and the autocalibration error across the simulated scenes, and a trend line for the single sample estimates. The trend shows that the standard deviation decreases with the square root of the number of accepted samples ($1/\sqrt{N_S}$).

The close match between standard deviation for the single ping estimates and the trend suggests that the number of accepted samples available essentially determine the error. This indicates that all accepted samples are equally suited for calibration, regardless of other factors like seafloor shape or noise level. However, these factors influence the number of accepted samples per ping. Scene 5, for example, has about 11 accepted samples per ping due to larger depth and

corresponding lower SNR. This is far below all the scenes at 40 m and about a tenth of the 97 accepted samples per ping for scene 7.

Fig. 7 also shows the root-mean-square (RMS) error across the array when calibrating on the complete 100-ping series. The RMS error is used since the mean value is unavailable with a single estimate. It includes a contribution of the bias, contrary to the standard deviation which removes it via the mean, and will therefore be higher. The amplitude RMS errors in Fig. 7 are about 0.01. Since this is similar to the scale of the mean amplitude error, and the predicted standard deviation is much smaller, our best explanation is that an amplitude bias dominates the amplitude RMS errors. The phase RMS error follows the trend line fairly closely, which indicates continued improvement in accuracy and lower bias for the phase estimation.

The calibration error model has no dependence on signal direction. Therefore, it is reasonable to expect that location of the calibration samples do not change the error greatly. To check this, we grouped the accepted samples in two ways and compared the resulting error in the calibration estimate. First, we grouped samples along-track, such that the accepted samples in the first few pings form the first group and so on. Then, we grouped samples across-track, such that the accepted samples furthest to port form the first group and so on. All groups had approximately the same size. We found the standard deviation with across-track grouping to be comparable but slightly higher. The increase was about 10 % for phase and 30 % for amplitude.

VII. Field results

Fig. 8 and 9 show the effect of autocalibration on two state-of-the-art swath sonar systems. Both systems were new, with first use shortly before our data were collected. Channel data were logged while operating the system in a normal mode using a tool provided by the manufacturer. The data was processed the same way as the simulated data. In both cases we have calibrated on all accepted samples from a set of sequential pings. The resulting calibration values were used to correct data from a separate line, to ensure no overlap between calibration and validation data. Below we show selected results representative of the cases we have examined.

Fig. 8 shows results from a system comparable to the simulated system. The data was collected near Sidney, British Columbia, Canada. Only one side is shown, as the receiver head was tilted 35 degrees. We used a $101\mu s$ pulse with center frequency 320 kHz. The nominal TX beamwidth at this frequency is 0.5 degrees. Autocalibration was done on 23606 accepted samples from 163 pings, collected the day after the ping shown.

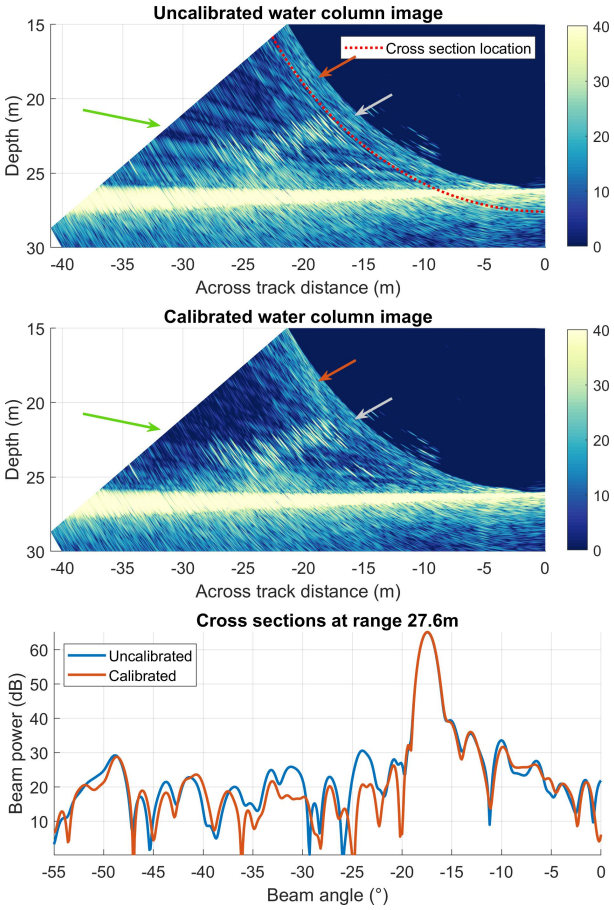

Fig. 8. Water column and cross section for 320 kHz field example. Flat seafloor with, presumably, a school of fish at about 20 to 25 m depth and -27 to -17 m across-track distance. Autocalibrated on 23606 accepted samples from 163 pings. The color scale show beam power in dB, with range clipped above to show sidelobes better. Arrows indicate example areas with reduced (green), essentially unchanged (grey), and increased (red) sidelobe levels. Data courtesy of the Canadian Hydrographic Service.

Much of the sidelobes surrounding the school of fish in Fig. 8 are suppressed better after autocalibration, especially to the left side indicated by a green arrow. This separates the school of fish better from the background. In other parts of the water column image sidelobes are roughly the same, and occasionally higher. One example of each are indicated by a grey and a red arrow, respectively.

In the cross section we also see the same effects. Without calibration the highest sidelobes are at about 30-35 dB. With calibration most sidelobes are reduced by at least 2 dB, approximately 10 dB at most. As in the water column some sidelobes are increased, at most by 2 dB. The

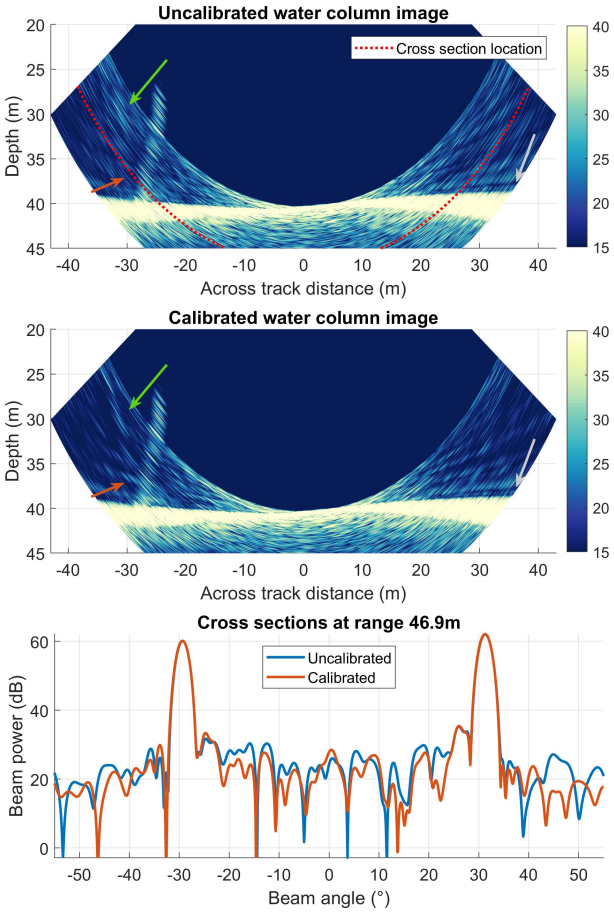

Fig. 9. Water column and cross section for 260 kHz field example with an artificial bubble flare. Autocalibrated on 8205 accepted samples from 91 pings. The color scale show beam power in dB, with range clipped above to show sidelobes better. Arrows indicate example areas with reduced (green), essentially unchanged (grey), and increased (red) sidelobe levels. Data courtesy of CCOM/JHC at the University of New Hampshire.

average sidelobe power[1] is initially at -38.6 dB and reduced by 1.1 dB after calibration. Note that the echo levels of the seafloor are essentially unchanged.

Fig. 9 shows results from a system similar, but smaller than, the previous. It has approximately 40 % larger receiver beamwidth. The data was collected outside Portsmouth, New Hampshire, USA. We used a 101 μs pulse with center frequency 260 kHz. The nominal TX beamwidth at this frequency is 1.5 degrees. We used 8205 accepted samples from 91 pings collected shortly

[1]Defined as the average power outside the minimums closest to the mainlobe in the uncalibrated case, relative to the peak. The same regions were used for the calibrated case. Note that there are two mainlobes due to the seafloor in the next example (Fig. 9), and both were excluded.

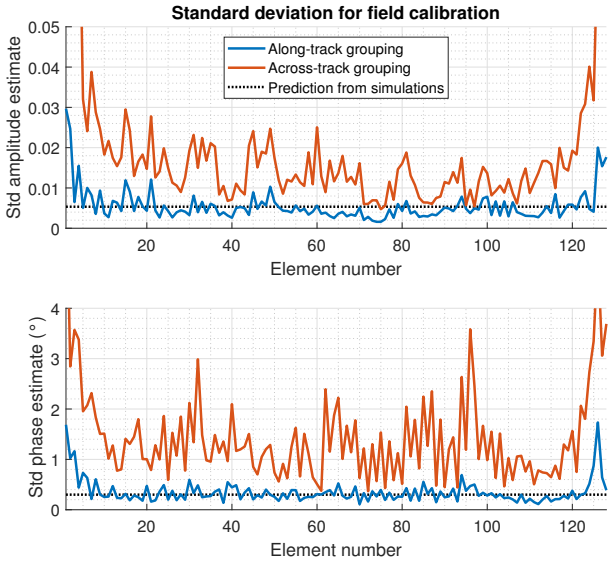

Fig. 10. Consistency checks for data used in calibration in Fig. 8. All accepted samples were divided into 10 groups of approximately 2360 samples in two ways, by along-track and across-track position. The GIAR autocalibration was run on each group and observed standard deviation (std) is shown. The predicted standard deviation is calculated using the fitted lines from Fig. 7.

before the ping shown for calibration. A bubble flare from a controlled seep is included to the left in Fig. 9. The seep generation device is described in [39].

The water column images in Fig. 9 show similar features as in the previous example. There are areas with reduced, roughly unchanged, and increased sidelobe level. Examples are indicated with a green, grey, and red arrow, respectively.

In the highlighted cross section most sidelobes are reduced by at least 2 dB, at best by over 10 dB. The sidelobe level is increased in some cases, at worst by almost 4 dB. The average sidelobe power is initially -36.4 dB. After calibration it is 1.3 dB lower. The echo level of the seafloor is essentially unchanged.

We do not think ambient noise is important for the performance in either field example due to a few reasons, although high noise level can reduce the benefit of lower sidelobes. The power in the water column is much higher for all angles after the first bottom echo, even though there is no reason that the level of ambient noise should change then. We see partially large suppression of sidelobes after the first bottom echo, even though calibration does not suppress noise. There also is a large dynamic range in the sidelobe region, while it should be more homogeneous if it was dominated by noise.

As for the simulated data, we ran calibration with different grouping of samples to investigate dependence on sample location. The calibration samples used for Fig. 8 were grouped by across-track position, in addition to the along-track grouping used before. Fig. 10 shows the estimated standard deviation for both grouping methods, together with the value expected from the simulations.

The values from along-track grouping and simulations are similar. However, the standard deviations when using across-track grouping are 3-4 times higher. This is much higher than the 10-30% increase we found in the corresponding experiment for the simulated data. We attribute this to a different nature of the calibration errors in the field than in the simulations. To mitigate this, we tested several extensions including geometric displacements and sectorwise calibration. None of the extensions improved performance significantly.

VIII. Discussion & conclusion

We have investigated if it is possible to reduce receiver sidelobes of swath sonars via autocalibration on data from normal operation. A method based on the "Generalized Interferometric Array Response" (GIAR) was used to find element-wise phase and amplitude calibration errors.

The accurate estimation of calibration errors in the simulations, and the stable error estimates across ping groups in the field, suggest that GIAR autocalibration reliably estimate some properties of the system. We achieve sidelobes below -50 dB in the simulations, which shows that this can lead to large performance improvements if the calibration model is accurate. The sidelobe reductions in the field indicates that practical improvements are possible. However, the reduced scale and variability of the field improvements, together with the lack of across-track consistency, show that an extended calibration model is needed. Based on the lack of improvement with the extensions we tested and related experience we expect that finding an appropriate model will be a challenging problem. Note that material and construction method may affect the nature of the calibration errors, so it is possible that different systems need different calibration models.

A new calibration model will require an updated method for correcting for the estimated errors, which may have increased computational demands. However, sample selection and maximizing GIAR are independent of the calibration model, and may therefore be unchanged. GIAR sample selection uses the same base data as traditional DAS and has a comparable computational load, it should therefore be relatively easy to use without interfering with other uses of the swath sonars. Based on these simulations we expect that GIAR will be able to collect calibration samples when

normal operations are possible. Bad conditions, as low SNR, will decrease the rate of accepted samples. However, samples with acceptable $|R|$ should exist as long as the SNR is high enough for useful data to be collected.

We see finding a suitable calibration model as the key issue for further research. It may also be interesting to apply this method to point targets, like calibration spheres [21], investigate effects of aging and environment changes, or if it is beneficial to combine autocalibration with adaptive beamformers. There is a need for comparable methods to reduce transmitter sidelobes, unfortunately our method is not well suited for this. A key problem is that our method depends on the ability to test many calibration values on each ping, while only one value can be used per element per transmission.

ACKNOWLEDGMENTS

We thank the staff at the Center for Coastal and Ocean Mapping/Joint Hydrographic Center at the University of New Hampshire for support and many insightful discussions during and after the first author's research visit. Special thanks to A. Lyons, J. H. Clarke, G. Rice, T. Weber, G. Masetti and V. Schmidt. J. H. Clarke was central for acquiring the field data from Sidney. We also thank T. Weber for arranging the collection of the data from Portsmouth, to K. Rychert for making and operating the bubble maker, to V Schmidt and his team for lending the transducer, and to T. Weber, K. Rychert, A. Padilla, T. Lyons, E. Weidner, E. Terry and M. Rowell for helping during data collection. G. Rice provided the Pydro par.py module which was helpful during data processing [40]. We also thank Kongsberg Maritime AS for assistance and feedback, particularly B. B. Berg. We thank the Canadian Hydrographic Service for the use of field data. We also acknowledge the reviewers for many comments and corrections that have improved this manuscript, and thank K. E. Wage and A. Hanssen for improvement suggestions provided as part of the evaluation of T. I. B. Lønmo's thesis.

REFERENCES

[1] J. E. H. Clarke, "Applications of multibeam water column imaging for hydrographic survey," *The Hydrographic Journal*, vol. 120, pp. 3–15, Apr. 2006. [Online]. Available: http://www.omg.unb.ca/omg/papers/HJ_water_column_JHC.pdf

[2] K. Nakamura, S. Kawagucci, K. Kitada, H. Kumagai, K. Takai, and K. Okino, "Water column imaging with multibeam echo-sounding in the mid-okinawa trough: Implications for distribution of deep-sea hydrothermal vent sites and the cause of acoustic water column anomaly," *Geochemical Journal*, vol. 49, no. 6, pp. 579–596, 2015.

[3] G. A. Mitchell, D. L. Orange, J. J. Gharib, and P. Kennedy, "Improved detection and mapping of deepwater hydrocarbon seeps: optimizing multibeam echosounder seafloor backscatter acquisition and processing techniques," *Marine Geophysical Research*, vol. 39, no. 1-2, pp. 323–347, Feb. 2018.

[4] J. E. H. Clarke, "Coherent refraction "noise" in multibeam data due to oceanographic turbulence," in *Proceedings of the U.S. Hydrographic Conference 2017*, Galveston, Texas, USA, Mar. 2017.

[5] C. de Moustier, "Signal processing for swath bathymetry and concurrent seafloor acoustic imaging," in *Acoustic Signal Processing for Ocean Exploration*, ser. NATO ASI Series, J. M. F. Moura and I. M. G. Lourtie, Eds. Springer Netherlands, 1993, vol. 388, pp. 329–354. [Online]. Available: http://jhc.unh.edu/sites/default/files/publications/deMoustier_93_ASPOE_Signal_Processing_Swath_Bathymetry_Concurrent_Acoustic_Imaging.pdf

[6] D. L. d. S. Pereira and J. E. H. Clarke, "Improving shallow water multibeam target detection at low grazing angles," in *U.S. Hydrographic Conference 2015*, National Harbor, Maryland U.S.A., Mar. 2015. [Online]. Available: http://www.omg.unb.ca/omg/papers/DouglasPereira_and_JHC_USHC2015_Paper.pdf

[7] X. Lurton, *An Introduction to Underwater Acoustics: Principles and Applications*, 2nd ed., ser. Geophysical Sciences. Springer-Verlag Berlin Heidelberg, 2010.

[8] F. J. Harris, "On the use of windows for harmonic analysis with the discrete Fourier transform," *Proceedings of the IEEE*, vol. 66, no. 1, pp. 51–83, Jan. 1978.

[9] J. Litva and T. K.-Y. Lo, *Digital Beamforming in Wireless Communications*, ser. Mobile Communications. Artech House, Aug. 1996.

[10] B. D. Steinberg, *Principles of aperture and array system design: Including random and adaptive arrays*. John Wiley & Sons, 1976.

[11] J. L. Butler and C. H. Sherman, *Transducers and Arrays for Underwater Sound*, 2nd ed., ser. Modern Acoustics and Signal Processing. Springer Nature, Sep. 2016.

[12] M. Viberg, M. Lanne, and A. Lundgren, "Calibration in array processing," in *Classical and Modern Direction-of-Arrival Estimation*. Academic Press, 2009, pp. 93–124.

[13] H. Krim and M. Viberg, "Two decades of array signal processing research: the parametric approach," *IEEE Signal Processing Magazine*, vol. 13, no. 4, pp. 67–94, Jul. 1996.

[14] T. I. B. Lønmo, A. Austeng, and R. E. Hansen, "Improving swath sonar water column imagery and bathymetry with adaptive beamforming," *IEEE Journal of Oceanic Engineering*, vol. 45, no. 4, Oct. 2020.

[15] H. L. Van Trees, *Optimum Array Processing*, ser. Detection, Estimation, and Modulation Theory. Wiley-Interscience, 2002, vol. 4.

[16] T. I. B. Lønmo, A. Austeng, and R. E. Hansen, "Interference rejection by low complexity adaptive beamforming," in *Seabed and Sediment Acoustics: Measurements and Modelling*, ser. Proceedings of the Institute of Acoustics, vol. 37, no. 1. Bath, United Kingdom: Institute of Acoustics, Sep. 2015. [Online]. Available: http://www.proceedings.com/27961.html

[17] ——, "Low complexity adaptive beamforming applied to sonar imaging (invited)," in *Proceedings of the 3rd International Conference and Exhibition on Underwater Acoustics*, J. S. Papadakis and L. Bjørnø, Eds., Crete, Greece, Jun. 2015, pp. 653–658. [Online]. Available: http://www.uaconferences.org/docs/Past_proceedings/UACE2015_Proceedings.pdf

[18] J. E. H. Clarke, "Dynamic motion and residuals in swath and sonar data: Ironing out the creases," *International Hydrographic Review*, vol. 4, no. 1, pp. 6–23, Mar. 2003. [Online]. Available: https://journals.lib.unb.ca/index.php/ihr/article/view/20600

[19] D. Guériot, J. Chèdru, S. Daniel, and E. Maillard, "The patch test: a comprehensive calibration tool for multibeam echosounders," in *Proceedings of OEANS 2000 MTS/IEEE Conference and Exhibition*, vol. 3, Sep. 2000, pp. 1655–1661 vol.3.

[20] G. Lamarche and X. Lurton, "Recommendations for improved and coherent acquisition and processing of backscatter data from seafloor-mapping sonars," *Marine Geophysical Research*, vol. 39, no. 1-2, pp. 5–22, May 2017.

[21] K. G. Foote, D. Chu, T. R. Hammar, K. C. Baldwin, L. A. Mayer, L. C. Hufnagle, Jr., and J. M. Jech, "Protocols for calibrating multibeam sonar," *The Journal of the Acoustical Society of America*, vol. 117, no. 4, pp. 2013–2027, Apr. 2005.

[22] Y. Li and M. H. Er, "Theoretical analyses of gain and phase error calibration with optimal implementation for linear equispaced array," *IEEE Transactions on Signal Processing*, vol. 54, no. 2, pp. 712–723, Feb. 2006.

[23] L. Qiong, G. Long, and Y. Zhongfu, "An overview of self-calibration in sensor array processing," in *Proceedings of 6th International Symposium on Antennas, Propagation and EM Theory (ISAPE'03)*, Beijing, China, Oct. 2003, pp. 279–282.

[24] J. C. Lanzoni and T. C. Weber, "Calibration of multibeam echo sounders: a comparison between two methodologies," in *European Conference on Underwater Acoustics*. Acoustical Society of America, 2012.

[25] X. Lurton and G. Lamarche, Eds., *Backscatter measurements by seafloor-mapping sonars: Guidelines and Recommendations*. GeoHab Backscatter Working Group, 2015. [Online]. Available: http://geohab.org/wp-content/uploads/2013/02/BWSG-REPORT-MAY2015.pdf

[26] P. Pocwiardowski, G. Yufit, E. Maillard, and P. Eriksen, "Method for large sonar calibration and backscattering strength estimation," in *OCEANS 2006*. Boston, MA, USA: IEEE, Sep. 2006.

[27] B. P. Ng, M. H. Er, and C. Kot, "Array gain/phase calibration techniques for adaptive beamforming and direction finding," *IEE Proceedings - Radar, Sonar and Navigation*, vol. 141, no. 1, pp. 25–29, Feb. 1994.

[28] P. Cervenka, "New processing schemes for multi-beam echo-sounders based on the generalized interferometric array response (invited)," in *Proceedings of 3rd International Conference and Exhibition on Underwater Acoustics*, J. S. Papadakis and L. Bjørnø, Eds., Crete, Greece, Jun. 2015, pp. 635–640. [Online]. Available: http://www.uaconferences.org/docs/Past_proceedings/UACE2015_Proceedings.pdf

[29] G. Farquharson, P. Lopez-Dekker, and S. J. Frasier, "Contrast-based phase calibration for remote sensing systems with digital beamforming antennas," *IEEE Transactions on Geoscience and Remote Sensing*, vol. 51, no. 3, pp. 1744–1754, Mar. 2013.

[30] D. H. Johnson and D. E. Dudgeon, *Array signal processing: Concepts and techniques*, ser. Prentice-Hall signal processing series. Prentice Hall, 1993.

[31] P. Cervenka, "A generalized interferometric array response. application to bathymetry with multi-beam echo-sounders (invited)," in *Proceedings of 3rd International Conference and Exhibition on Underwater Acoustics*, J. S. Papadakis and L. Bjørnø, Eds., Crete, Greece, Jun. 2015, pp. 629–634. [Online]. Available: http://www.uaconferences.org/docs/Past_proceedings/UACE2015_Proceedings.pdf

[32] K. W. Hollman, K. W. Rigby, and M. O'Donnell, "Coherence factor of speckle from a multi-row probe," in *Proceedings of IEEE Ultrasonics Symposium*, vol. 2, Caesars Tahoe, NV, USA, Oct. 1999, pp. 1257–1260.

[33] N. S. Neidell and M. T. Taner, "Semblance and other coherency measures for multichannel data," *GEOPHYSICS*, vol. 36, no. 3, pp. 482–497, Jun. 1971.

[34] MATLAB, *version 9.5.0.944444 (R2018a)*. Natick, Massachusetts: The MathWorks Inc., 2010.

[35] J. A. Jensen and N. B. Svendsen, "Calculation of pressure fields from arbitrarily shaped, apodized, and excited ultrasound transducers," *IEEE Transactions on Ultrasonics, Ferroelectrics, and Frequency Control*, vol. 39, no. 2, pp. 262–267, Mar. 1992.

[36] J. A. Jensen, "Field: A program for simulating ultrasound systems," in *Medical & Biological Engineering & Computing*, vol. 34, no. SUPPL. 1, 1996, pp. 351–353. [Online]. Available: http://field-ii.dk/documents/jaj_nbc_1996.pdf

[37] A. Blachet, T. I. B. Lønmo, A. Austeng, F. Prieur, A. J. Hunter, and R. E. Hansen, "Sonar data simulation with application to multi-beam echo sounders," in *Proceedings of 4th Underwater Acoustics Conference and Exhibition*, Skiathos, Greece,

Sep. 2017. [Online]. Available: http://www.uaconferences.org/index.php/component/contentbuilder/details/9/36/uace2017-sonar-data-simulation-with-application-to-multi-beam-echo-sounders?Itemid=410

[38] R. E. Walpole, R. H. Myers, S. L. Myers, and K. Ye, *Probability and Statistics for Engineers and Scientists*. Pearson Prentice Hall, 2007. [Online]. Available: http://books.google.no/books?id=k6etQgAACAAJ

[39] K. M. Rychert and T. C. Weber, "Tests of acoustic target strength and bubble dissolution models using a synthetic bubble generator," *Journal of Atmospheric and Oceanic Technology*, Dec. 2019.

[40] G. Rice, "Pydro par.py module v0.3.8," Computer software, 2017, available from https://nauticalcharts.noaa.gov/data/tools-apps.html.

[41] J. S. Papadakis and L. Bjørnø, Eds., *Proceedings of 3rd Underwater Acoustics Conference and Exhibition*, Crete, Greece, Jun. 2015. [Online]. Available: http://www.uaconferences.org/docs/Past_proceedings/UACE2015_Proceedings.pdf

Tor Inge Birkenes Lønmo (M'19) received the M.Sc. degree in education with specialization in physics and mathematics from the Norwegian University of Science and Technology (NTNU), Trondheim, Norway in 2012, and the Ph.D. degree in signal processing at the University of Oslo, Norway in 2020. His Ph.D. thesis was entitled "Adaptive Beamforming and Autocalibration for Swath Sonars". Since 2012 he has been working with signal processing for sonars at Kongsberg Maritime AS, Horten, Norway. He has also worked on signal processing for radar at the Norwegian Defence Research Establishment (FFI) (2010, 2011, 2012). His research interests include signal processing for acoustical underwater arrays and array modeling.

Andreas Austeng (S'97–M'01-SM'16) received the M.S. degree in physics and the Ph.D. degree in computer science from the University of Oslo, Norway, in 1996 and in 2001, respectively. Since 2001, he has been working at the Department of Informatics, University of Oslo, as a postdoctoral research fellow, an Associate Professor, and currently as a Professor with the Digital Signal Processing and Image Analysis Group. His research interests include signal processing for acoustical imaging and algorithms that aim to improve the quality or the information extracted from images.

Roy Edgar Hansen (M'07-SM'16) received the M.Sc. degree in physics in 1992, and the Ph.D. degree in physics in 1999, both from the University of Tromsø, Norway. His Ph.D. thesis was entitled Measurements in the Mixed Layer by a Bistatic Multi-CW Doppler Sonar.

From 1992 to 2000 he was with the Norwegian research company TRIAD, working on multistatic sonar, multistatic radar, SAR and underwater communications. Since 2000, he has been working at the Norwegian Defence Research Establishment (FFI), Kjeller, Norway, in the field of synthetic aperture sonar. He is currently Principal Scientist at FFI. He is also Adjunct Professor in acoustic imaging at the Department of Informatics at University in Oslo, Norway. His research interests include synthetic aperture sonar and radar, ultrasound imaging, sonar signal processing and array signal processing.